JOURNAL OF SYNCHROTRON RADIATION
ISSN 1600-5775

Development and application of a tender X-ray ptychographic coherent diffraction imaging system on BL27SU at SPring-8

Masaki Abe,[a,b,d,e]* Fusae Kaneko,[c,e] Nozomu Ishiguro,[b,d,e] Togo Kudo,[b,f] Takahiro Matsumoto,[f] Takaki Hatsui,[b,f] Yusuke Tamenori,[f] Hiroyuki Kishimoto[c] and Yukio Takahashi[b,d,e]*

Received 26 February 2021
Accepted 17 June 2021

Edited by M. Yamamoto, RIKEN SPring-8 Center, Japan

Keywords: ptychographic coherent diffraction imaging; CDI; tender X-rays; sulfur materials.

[a]Department of Metallurgy, Materials Science and Materials Processing, Graduate School of Engineering, Tohoku University, Aoba-yama 02, Aoba-ku, Sendai 980-8579, Japan, [b]RIKEN SPring-8 Center, 1-1-1 Kouto, Sayo-cho, Sayo-gun, Hyogo 679-5148, Japan, [c]Sumitomo Rubber Industries, Ltd., 2-1-1 Tsutsui, Chuo, Kobe, Hyogo 651-0071, Japan, [d]International Center for Synchrotron Radiation Innovation Smart (SRIS), Tohoku University, 2-1-1 Katahira, Aoba-ku, Sendai 980-8577, Japan, [e]Institute of Multidisciplinary Research for Advanced Materials (IMRAM), Tohoku University, 2-1-1 Katahira, Aoba-ku, Sendai 980-8577, Japan, and [f]Japan Synchrotron Radiation Research Institute (JASRI), Kouto 1-1-1, Sayo-cho, Sayo-gun, Hyogo 679-5198, Japan. *Correspondence e-mail: masaki.abe.p1@dc.tohoku.ac.jp, ytakahashi@tohoku.ac.jp

Ptychographic coherent diffraction imaging (CDI) allows the visualization of both the structure and chemical state of materials on the nanoscale, and has been developed for use in the soft and hard X-ray regions. In this study, a ptychographic CDI system with pinhole or Fresnel zone-plate optics for use in the tender X-ray region (2–5 keV) was developed on beamline BL27SU at SPring-8, in which high-precision pinholes optimized for the tender energy range were used to obtain diffraction intensity patterns with a low background, and a temperature stabilization system was developed to reduce the drift of the sample position. A ptychography measurement of a 200 nm thick tantalum test chart was performed at an incident X-ray energy of 2.500 keV, and the phase image of the test chart was successfully reconstructed with approximately 50 nm resolution. As an application to practical materials, a sulfur polymer material was measured in the range of 2.465 to 2.500 keV including the sulfur *K* absorption edge, and the phase and absorption images were successfully reconstructed and the nanoscale absorption/phase spectra were derived from images at multiple energies. In 3 GeV synchrotron radiation facilities with a low-emittance storage ring, the use of the present system will allow the visualization on the nanoscale of the chemical states of various light elements that play important roles in materials science, biology and environmental science.

1. Introduction

The tender energy range of 2 to 5 keV, between the energy ranges of soft and hard X-rays, covers the *K* absorption edge of 3*p* elements, such as sulfur (S) and phosphorus (P), which play important roles in materials science, biology and environmental science, such as MoS_2 catalysts (Jaramillo *et al.*, 2007), Li–S batteries (Kim *et al.*, 2013) and phosphorus compounds in living organisms. Many of these practical materials and biological specimens are heterogeneous and complex systems, and hence it is necessary to observe their structures and chemical states over a wide range of several micrometres with nanoscale spatial resolution and to understand their functions. Lens-based X-ray microscopy techniques such as scanning transmission X-ray microscopy (STXM) (Xiao *et al.*, 2017), full-field transmission X-ray microscopy (TXM) (Salomé *et al.*, 2000) and micro X-ray fluorescence (Tamenori *et al.*, 2011) in the tender energy range are

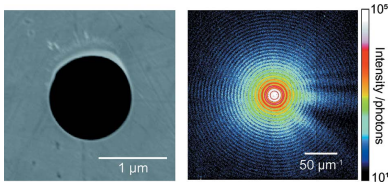

promising tools for observing structures and analyzing chemical states on the submicrometre scale. In recent years, there has been a growing demand for observation with even higher spatial resolution. For example, elemental zoning in an alumina-supported cobalt molybdenum sulfide catalyst has been visualized at sub-50 nm resolution by STXM (Samarai *et al.*, 2015). Currently, the spatial resolution is approaching the limit due to the fabrication accuracy of the lens.

Coherent diffraction imaging (CDI) is a lensless microscopy technique that can achieve a spatial resolution beyond the performance limit of a lens (Chapman & Nugent, 2010; Miao *et al.*, 2015). In CDI, a sample is illuminated with coherent light and the sample image is reconstructed by performing phase-retrieval calculations on the diffraction intensity pattern. In particular, scanning CDI, *i.e.* ptychographic CDI, with both a wide field of view and a high spatial resolution, is applicable to various samples (Rodenburg *et al.*, 2007; Pfeiffer, 2018). Thus far, ptychographic CDI measurement systems have been developed at synchrotron radiation facilities, especially for use in the soft (Shapiro *et al.*, 2020) and hard (Takahashi *et al.*, 2011; Holler *et al.*, 2014; Deng *et al.*, 2019; Schropp *et al.*, 2020) X-ray regions, and have been applied to the structural imaging of biological specimens (Deng *et al.*, 2015) and functional materials (Ihli *et al.*, 2020). Ptychographic CDI has also been extended to the visualization of chemical states using X-ray absorption edges (Shapiro *et al.*, 2014; Hirose *et al.*, 2018), which is called spectro-ptychography or the ptychographic X-ray absorption fine structure (XAFS) method. Ptychographic CDI could also be applied to the observation of various samples in the tender energy range, but there are no reports of this yet because there are only a few synchrotron radiation beamlines that can use high-brilliance tender X-rays.

The BL27SU beamline (Ohashi *et al.*, 2001) at SPring-8 is one of the few synchrotron radiation beamlines that provide high-brilliance tender X-rays, in which a quasi-monochromatic beam emitted from a figure-8 undulator is monochromated by high-order harmonic removal mirrors and an Si111 channel-cut monochromator, and tender X-rays between 2.1 and 3.3 keV are available in the B branch. In addition, the BL27SU beamline is equipped with a differential pumping system, and hence windowless experiments can be performed under normal atmospheric conditions (Tamenori, 2010). In this study, a tender X-ray ptychographic CDI system is developed on the BL27SU beamline, in which a high-precision pinhole fabrication technique and a temperature stabilization system are developed, and pinhole optics or Fresnel zone-plate (FZP) optics are installed with a low-vacuum chamber. The performance of the system is evaluated by measuring a test sample and a practical material.

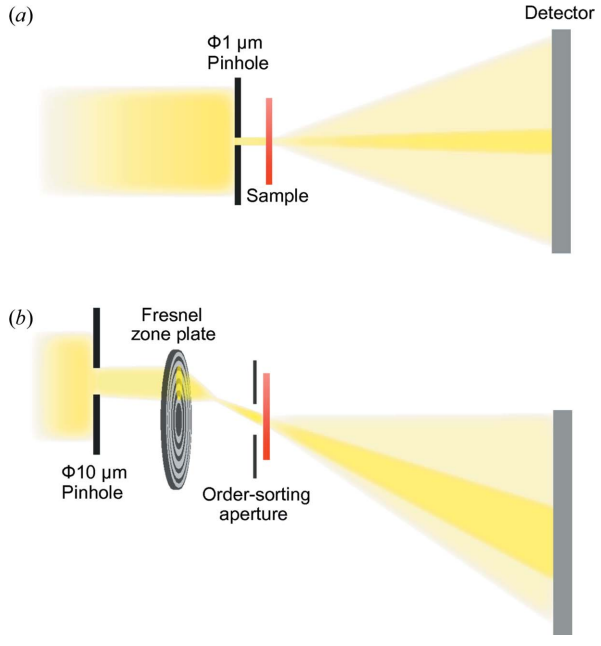

Figure 1
Schematic diagrams of tender X-ray ptychographic CDI optics developed on the BL27SU beamline at SPring-8. (*a*) Pinhole optics. (*b*) Fresnel zone-plate optics.

2. Development of a ptychographic CDI measurement system for use in the tender X-ray region

2.1. Design of ptychographic CDI optics

Figs. 1(*a*) and 1(*b*) show schematic diagrams of pinhole optics and FZP optics for tender X-ray ptychographic CDI developed on the BL27SU beamline at SPring-8. In the pinhole optics, X-rays are irradiated through a pinhole of 1 μm diameter and the X-rays passing through the pinhole are irradiated onto a sample to measure the far-field diffraction intensity pattern. Diffraction patterns were acquired using a direct-detection X-ray SOI-CMOS imaging detector, SOPHIAS-L (1.9 Mpixels, 30 μm square pixels, imaging area of 26.7 mm × 64.8 mm). The detector consists of a sensor that is a lower-noise circuitry version of the previously reported sensor, SOPHIAS (Hatsui *et al.*, 2013). The detector system showed a system noise of 67 e r.m.s. The sensor has an integrating-type pixel (Hatsui & Graafsma, 2015) and was operated at 30 frames s^{-1} at −20°C with a bias voltage of 200 V. The sensor has a silicon photodiode with a thickness of 500 μm, made from an *n*-type floating-zone silicon ingot with a resistivity of 5.2 to 6.2 kΩ. Flat-field and dark corrections were carried out. Flat-field images were measured before the synchrotron radiation experiments using an X-ray source with a copper target (Hamamatsu Photonics KK, L9631-33). The pre-sampled point-spread function of the signal charge was evaluated to be about 20 μm FWHM using an optical method described elsewhere (Nakajima *et al.*, 2021). The spread of the signal charge, comparable with the physical pixel size, means the majority of single-photon events are shared by at most 3 × 3 pixels. In order to achieve single-photon sensitivity and a linear response of the detector, such events were processed so that the nearby charges were moved to the pixel with the most intense signal in a 3 × 3 pixel matrix. Other weak events with all pixels in the 3 × 3 pixel matrix showing a signal less than 300 e were considered detector noise and suppressed to

zeros. The above data processing provided a photon energy resolution of 1.07 keV FWHM for 2.5 keV photons, successfully distinguishing 2.5 keV photons from the noise floor of the detector. The distance between the pinhole and the sample was 0.8 mm, and the distance between the sample and the detector was 1.31 m.

In the FZP optics, in order to optimize the number of scanning points with respect to the sample size, the beam size at the sample position was designed to be ∼1 µm, the same as the pinhole optics. A pinhole of 10 µm diameter was reduced to a tenth of its original size by an FZP with a nickel thickness of 900 nm, a minimum zone width of 50 nm and an outer diameter of 180 µm (Applied Nanotools Inc.). The focal length of the FZP was 18.15 mm at 2.500 keV. The distance between the pinhole and the FZP was 199.64 mm and the distance between the FZP and the sample surface was 19.96 mm. The diffraction efficiency of the first-order focus at 2.500 keV is estimated to be ∼28%. The FZP optics can be expected to have a more than ten times larger incident flux than the pinhole optics. The FZP was located 50 µm off-axis laterally to the aperture beam so that the pinhole illumination was incident outside the optics to separate the first-order focus from the direct beam. A 20 µm square aperture in 200 µm thick silicon was used as the order-sorting aperture, which was placed immediately in front of the sample. The sample was attached to piezo stages (PI GmbH Co., P-621.ZLC and P-621.1CL) which are capable of translation movement in two axes (vertical/horizontal) in a plane perpendicular to the optical axis. In this system, the sample and all optical elements were placed in a vacuum chamber evacuated to approximately 1 Pa.

2.2. Fabrication and evaluation of the high-precision pinhole

In ptychography measurements, it is crucial to suppress parasitic scattering from the illumination optics to obtain diffraction intensity patterns with a low background. For pinhole optics, a high-precision pinhole is required in order to reduce the parasitic scattering from the pinhole inner wall. The material of the pinhole should be as thin as possible so that the transmission of X-rays outside the aperture is negligible, and the surface roughness of the inner wall of the aperture should be small. The high-precision pinhole for this work was fabricated as follows. A platinum (Pt) foil was polished on both sides to a thickness of 4 µm (TDC Co. Ltd, Miyagi, Japan) which is sufficiently thick to block tender X-rays. The transmittance of 2.500 keV X-rays to the Pt foil is estimated to be $\sim 4.7 \times 10^{-11}$. The Pt foils were fixed with aluminium jigs, and pinhole slits of 1 and 10 µm diameter were fabricated on the Pt films using a focused ion beam (FIB). Fig. 2(*a*) shows a scanning electron microscopy (SEM) image of the 1 µm pinhole. On the BL27SU beamline, the pinhole slits were irradiated with X-rays monochromated to 2.5 keV, and the diffraction intensity pattern [Fig. 2(*b*)] was measured 1.31 m downstream. A clear concentric pattern is observed to very high orders, indicating that the coherence of the X-rays irradiated through the pinhole is high and the pinhole has been processed with a low roughness on the inner wall and sharp edges. The anisotropic scattering on the right-hand side of the diffraction intensity pattern is due to the slight deviation of the pinhole shape from a perfect circle. The flux of X-rays after passing through the 1 µm pinhole was $\sim 1.7 \times 10^{7}$ photons s^{-1}.

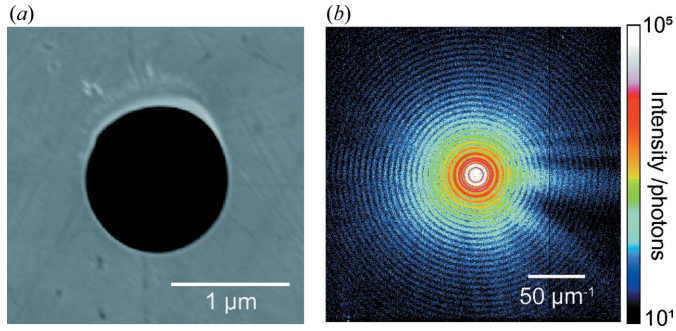

Figure 2
(*a*) An SEM image of the 1 µm pinhole fabricated by FIB processing on a Pt foil. (*b*) A coherent X-ray diffraction pattern from the pinhole.

2.3. Evaluation of the temperature stabilization system

Thermal stability of the optics is another critical factor for ptychography measurements. A temperature stabilization system for the optics of ptychographic CDI was constructed on the BL27SU beamline and Fig. 3(*a*) shows a photograph of the optical system. A high-order harmonic removal mirror, a monochromator, a sample chamber and a detector are surrounded by a vinyl booth, with the internal atmosphere temperature-controlled by precision air processors (ORION Co. Ltd, PAP03C). The air delivered by the air processors is set at 25°C and is stable within a range of ±0.1°C inside the vinyl booth. To evaluate the positional stability of the X-ray beam in the sample plane, the amount of drift was measured by the dark-field knife-edge scanning method with the edge of a test chart (Takahashi *et al.*, 2011).

Fig. 3(*b*) shows the time dependence of the beam position along the horizontal and vertical directions for the pinhole optics with and without temperature control, and for the FZP optics with temperature control. The amount of drift is significantly reduced by the temperature stabilization system. The amounts of drift for the pinhole optics without and with temperature control were, respectively, 4.3 µm and 920 nm in the horizontal direction and 8.9 µm and 2.9 µm in the vertical direction in 3 h. Using FZP optics, the drift was even smaller, 330 nm in the horizontal direction and 960 nm in the vertical direction. In the present FZP optical system, since the pinhole shape at the sample position is reduced in size, the beam drift at the imaging plane (sample position) is also expected to be reduced. However, the drift was still observed after 3 h of measurement. A stepping motor-driven translation stage was used in the coarse-positioning stage of the sample before the dark-field knife-edge scan, and the heat generated by the motor is thought to be the cause of the residual drift. To compensate for this drift, a system that uses laser inter-

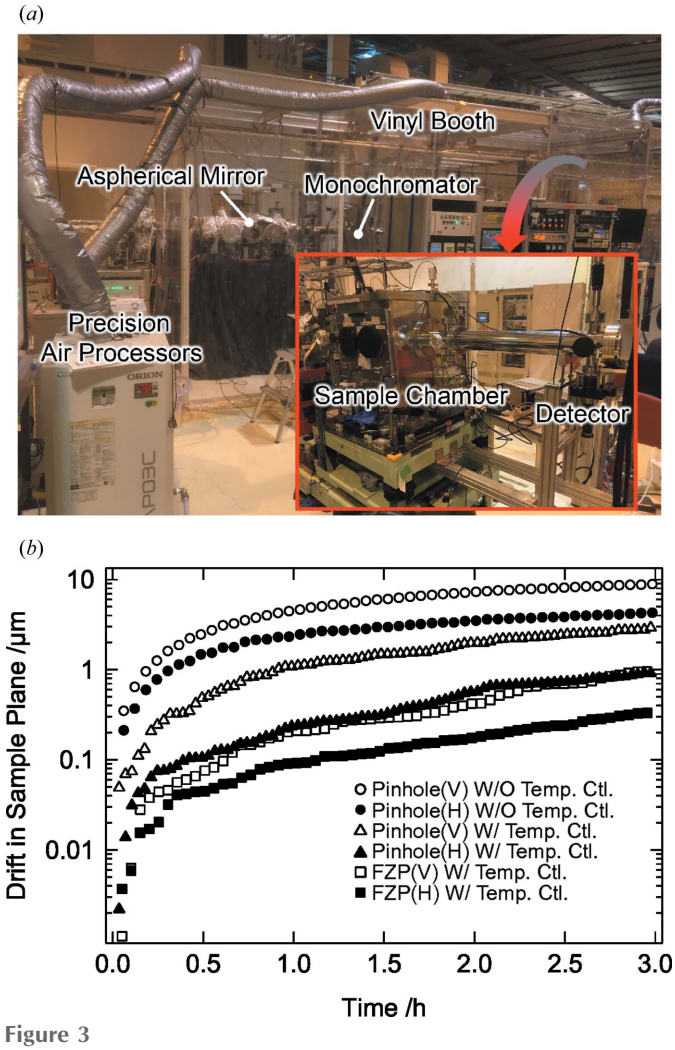

Figure 3
(*a*) A photograph of a tender X-ray ptychography measurement system installed with a temperature stabilization system on the BL27SU beamline at SPring-8. (*b*) The time dependence of the amount of drift of the beam position in the sample plane in the horizontal and vertical directions for pinhole optics with and without temperature control and for FZP optics with temperature control.

ferometry to compensate for the relative position of the sample and pinhole is being investigated (Nazaretski *et al.*, 2014).

3. Ptychography measurement and reconstruction

3.1. Ta test chart

X-ray ptychography measurements of a 200 nm thick tantalum (Ta) Siemens star pattern were carried out using 2.500 keV X-rays with the pinhole and FZP optics. The test chart was raster-scanned in 17 × 17 points for the pinhole optics and in 15 × 15 points for the FZP optics with a 500 nm step size. The sample position was corrected every two points in the pinhole optics and every 15 points in the FZP optics. The exposure times at each position were 25 s for the pinhole optics and 5 s for the FZP optics. Coherent X-ray diffraction patterns were captured by the SOPHIAS detector. The sample

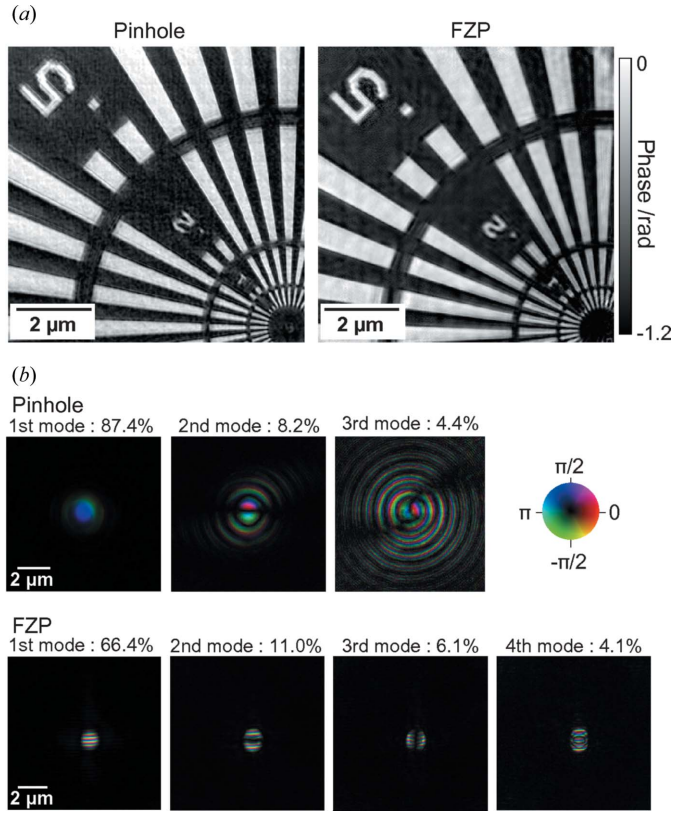

Figure 4
Images reconstructed from the ptychographic diffraction patterns measured using the pinhole optics and the FZP optics at 2.500 keV. (*a*) Phase images of the Ta test chart. (*b*) Amplitude images of the illumination field.

and probe images were reconstructed by the mixed-state reconstruction method (Thibault & Menzel, 2013). Figs. 4(*a*) and 4(*b*) show the reconstructed phase images of the test chart and amplitude images of the illumination field, respectively. The 50 nm minimum structures of the sample are clearly reconstructed for both optics. The illumination function was separated into three orthogonal modes for the pinhole optics and nine orthogonal modes for the FZP optics. The illumination fields of the FZP optics in Fig. 4(*b*) are the four most populated of the nine probe modes.

3.2. Sulfur polymer material

X-ray ptychography measurements of a sulfur polymer material were then performed. The sulfur polymer particles were prepared by mixing and sintering a polymer composed of carbon, oxygen and hydrogen with sulfur, and were then dispersed on an SiN membrane. Fig. 5(*a*) shows an SEM image of the measured particle. Ptychographic diffraction patterns were measured at eight energies, *i.e.* 2.465, 2.4692, 2.471, 2.4718, 2.4732, 2.4776, 2.481 and 2.500 keV, around the S *K* absorption edge with the FZP optics. For the energy calibration, the spectrum of $CaSO_4$ was used as a standard, setting the white-line maximum at 2.4819 keV (Michael, 2005). The sample was raster-scanned in 20 × 20 points with a 400 nm step size, and the position of the sample was corrected every

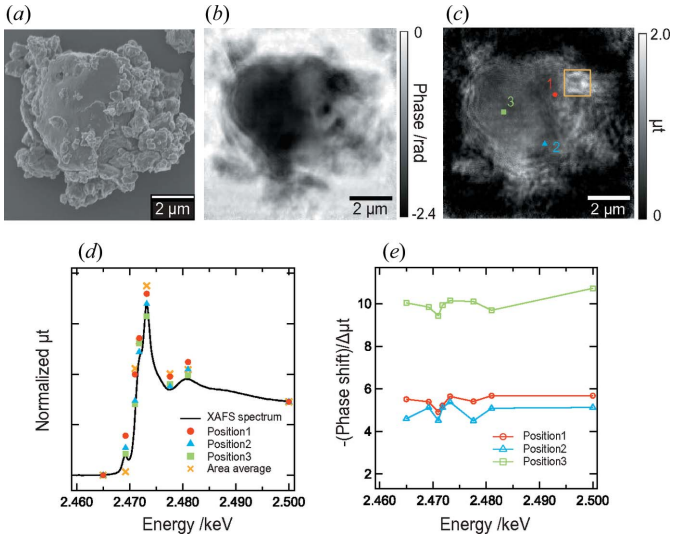

Figure 5
(*a*) An SEM image of the sulfur polymer material. (*b*), (*c*) Reconstructed images of the sulfur polymer material at 2.4732 keV, (*b*) phase image, (*c*) μt image. (*d*) Ptychographic XAFS spectra at positions 1, 2 and 3 and area average (25 × 25 pixels) in panel (*c*) and reference XAFS spectrum. (*e*) Phase spectrum normalized by $\Delta\mu t$ at positions 1, 2 and 3.

20 points. The exposure time at each position was 5 s. Figs. 5(*b*) and 5(*c*) show the reconstructed phase and absorption images at 2.4732 keV above the S *K* absorption edge, respectively, where the absorption image, *i.e.* the μt image, is derived based on $\mu t = -2\log|T|$, where T is the amplitude of the complex transmission function of the sample. The shapes of the particles are in good agreement with the SEM image. The intensity distributions in the phase and μt images do not match. Edge jumps ($\Delta\mu t$), the differences in μt between 2.465 and 2.500 keV, for three arbitrary positions (average of 2 × 2 pixels) and a selected area (average of 25 × 25 pixels) of Fig. 5(*c*) were estimated as 0.253, 0.247, 0.193 and 0.419, respectively. The selected white areas in the μt image are considered to be localized sulfur, as its $\Delta\mu t$ value is larger than those at the other three points. The intensities of the μt image normalized by $\Delta\mu t$ for the three positions and the selected area were then plotted together with the reference XAFS spectrum, as shown in Fig. 5(*d*), in which the reference XAFS spectrum was obtained by the total electron yield method for powder samples. The peak at 2.4718 keV is from the S—S bond, the peak at 2.4732 keV is from the S—C bond and the peak at 2.481 keV is from sulfate. The peak at an energy lower than 2.470 keV is considered to be attributable to the (S)1*s*(C═S)π^* transition, associated with the π-bonding of the C═S linkage (Yu *et al.*, 2001). The intensities of the μt images show a similar energy dependence to that of the XAFS spectrum. However, the quality of the reconstructed images is insufficient, making it difficult to analyze more detailed information such as the distribution of chemical species. In addition, the phase spectra normalized by $\Delta\mu t$ at the three positions were calculated, as shown in Fig. 5(*e*). The larger value of −(Phase shift)/$\Delta\mu t$ at position 3 compared with positions 1 and 2 suggests that the composition of position 3 is different from that of positions 1 and 2, and that it has more carbon. The mismatch between the intensity distributions of the phase and μt images can be considered to be due to the inhomogeneity of the composition.

4. Conclusions

We have developed a tender X-ray ptychographic CDI system with pinhole or FZP optics on the BL27SU beamline at SPring-8, in which we used a high-precision pinhole optimized for the tender energy range and introduced a temperature stabilization system. Using this system, we achieved a resolution of approximately 50 nm in ptychographic CDI of a 200 nm thick Ta test chart. In addition, a sulfur polymer material was measured at the S *K* edge, and the particle morphology and ptychographic XAFS spectra were successfully obtained.

At present, the spatial resolution of tender X-ray ptychographic CDI is limited by the fluence of incident coherent X-rays. In 3 GeV synchrotron radiation facilities with a low-emittance storage ring, which have been built or are under construction at several locations around the world, tender X-rays with higher brightness are or will be provided. For example, an advanced synchrotron radiation facility with a low-emittance 3 GeV synchrotron storage ring is being constructed in Japan (Takata *et al.*, 2019), where a few beamlines will provide tender X-rays that are tens of times brighter than those of the BL27SU beamline. In the near future, we will be able to achieve a higher spatial resolution than that of STXM with tender X-ray ptychographic CDI. We believe that tender X-ray ptychographic CDI will be a tool for elucidating the function of various elements that play important roles in materials science, biology and environmental science.

Acknowledgements

We thank Dr Makoto Hirose, Dr Ryo Mashita, Dr Tomomi Masui, Dr Hiroki Suga and Dr Kiyofumi Nitta for their help in the synchrotron experiments, and Mr Yusuke Kohashi and Mr Yoshiaki Honjo for their support in the detector developments.

Funding information

This work was supported by the Japan Society for the Promotion of Science (JSPS) KAKENHI (grant Nos. JP18H05253, JP19H05814, JP20K15375 and JP20K20523). This work was also supported in part by the 'Dynamic Alliance for Open Innovation Bridging Human, Environment and Materials' from the Ministry of Education, Culture, Sports, Science and Technology of Japan (MEXT). The X-ray ptychography experiments were performed on BL27SU at SPring-8 with the approval of the Japan Synchrotron Radiation Research Institute (JASRI) (Proposal Nos. 2018A1307, 2018B1303, 2019A0164, 2019B0164, 2020A0164, 2020A0629 and 2021A0164).

References

Chapman, H. N. & Nugent, K. A. (2010). *Nat. Photon.* **4**, 833–839.

Deng, J., Preissner, C., Klug, J. A., Mashrafi, S., Roehrig, C., Jiang, Y., Yao, Y., Wojcik, M., Wyman, M. D., Vine, D., Yue, K., Chen, S., Mooney, T., Wang, M., Feng, Z., Jin, D., Cai, Z., Lai, B. & Vogt, S. (2019). *Rev. Sci. Instrum.* **90**, 083701.

Deng, J., Vine, D. J., Chen, S., Nashed, Y. S. G., Jin, Q., Phillips, N. W., Peterka, T., Ross, R., Vogt, S. & Jacobsen, C. J. (2015). *Proc. Natl Acad. Sci. USA*, **112**, 2314–2319.

Hatsui, T. & Graafsma, H. (2015). *IUCrJ*, **2**, 371–383.

Hatsui, T., Omodani, M., Kudo, T., Kobayashi, K., Imamura, T., Ohmoto, T., Iwata, A., Ono, S., Kirihara, Y., Kameshima, T., Kasai, H., Miura, N., Kuriyama, N., Okihara, M., Nagatomo, Y., Nagasaki, M., Watanabe, T. & Yabashi, M. (2013). *Proceedings of the 2013 International Image Sensor Workshop (IISW)*, Article No. 3.05, 12–16 June 2013, Snowbird, Utah, USA.

Hirose, M., Ishiguro, N., Shimomura, K., Burdet, N., Matsui, H., Tada, M. & Takahashi, Y. (2018). *Angew. Chem.* **130**, 1490–1495.

Holler, M., Diaz, A., Guizar-Sicairos, M., Karvinen, P., Färm, E., Härkönen, E., Ritala, M., Menzel, A., Raabe, J. & Bunk, O. (2014). *Sci. Rep.* **4**, 3857.

Ihli, J., Bloch, L., Krumeich, F., Wakonig, K., Holler, M., Guizar-Sicairos, M., Weber, T., Silva, J. C. & Bokhoven, J. A. (2020). *Angew. Chem. Int. Ed.* **59**, 17266–17271.

Jaramillo, T. F., Jørgensen, K. P., Bonde, J., Nielsen, J. N., Horch, S. & Chorkendorff, I. (2007). *Science*, **317**, 100–102.

Kim, J., Lee, D.-J., Jung, H.-G., Sun, Y.-K., Hassoun, J. & Scrosati, B. (2013). *Adv. Funct. Mater.* **23**, 1076–1080.

Miao, J., Ishikawa, T., Robinson, I. K. & Murnane, M. M. (2015). *Science*, **348**, 530–535.

Michael, E. F. (2005). *Can. Mineral.* **43**, 1811–1838.

Nakajima, K., Kameshima, T. & Hatsui, T. (2021). *Nucl. Instrum. Methods Phys. Res. A*, **1003**, 165303.

Nazaretski, E., Huang, X., Yan, H., Lauer, K., Conley, R., Bouet, N., Zhou, J., Xu, W., Eom, D., Legnini, D., Harder, R., Lin, C.-H., Chen, Y.-S., Hwu, Y. & Chu, Y. S. (2014). *Rev. Sci. Instrum.* **85**, 033707.

Ohashi, H., Ishiguro, E., Tamenori, Y., Kishimoto, H., Tanaka, M., Irie, M., Tanaka, T. & Ishikawa, T. (2001). *Nucl. Instrum. Methods Phys. Res. A*, **467–468**, 529–532.

Pfeiffer, F. (2018). *Nat. Photon.* **12**, 9–17.

Rodenburg, J. M., Hurst, A. C., Cullis, A. G., Dobson, B. R., Pfeiffer, F., Bunk, O., David, C., Jefimovs, K. & Johnson, I. (2007). *Phys. Rev. Lett.* **98**, 034801.

Salomé, M., Lafage-Proust, M. H., Vico, L., Amblard, D., Kaulich, B., Oestreich, S., Susini, J. & Barrett, R. (2000). *AIP Conf. Proc.* **507**, 178–183.

Samarai, M. A., Meirer, F., Karunakaran, C., Wang, J., Vogt, E. T. C., Zandbergen, H. W., Weber, T., Weckhuysen, B. M. & de Groot, F. M. F. (2015). *J. Phys. Chem. C*, **119**, 2530–2536.

Schropp, A., Döhrmann, R., Botta, S., Brückner, D., Kahnt, M., Lyubomirskiy, M., Ossig, C., Scholz, M., Seyrich, M., Stuckelberger, M. E., Wiljes, P., Wittwer, F., Garrevoet, J., Falkenberg, G., Fam, Y., Sheppard, T. L., Grunwaldt, J.-D. & Schroer, C. G. (2020). *J. Appl. Cryst.* **53**, 957–971.

Shapiro, D. A., Babin, S., Celestre, R. S., Chao, W., Conley, R. P., Denes, P., Enders, B., Enfedaque, P., James, S., Joseph, J. W., Krishnan, H., Marchesini, S., Muriki, K., Nowrouzi, K., Oh, S. R., Padmore, H., Warwick, T., Yang, L., Yashchuk, V. V., Yu, Y.-S. & Zhao, J. (2020). *Sci. Adv.* **6**, eabc4904.

Shapiro, D. A., Yu, Y.-S., Tyliszczak, T., Cabana, J., Celestre, R., Chao, W., Kaznatcheev, K., Kilcoyne, A. L. D., Maia, F., Marchesini, S., Meng, Y. S., Warwick, T., Yang, L. L. & Padmore, H. A. (2014). *Nat. Photon.* **8**, 765–769.

Takahashi, Y., Suzuki, A., Zettsu, N., Kohmura, Y., Senba, Y., Ohashi, H., Yamauchi, K. & Ishikawa, T. (2011). *Phys. Rev. B*, **83**, 214109.

Takata, M., Maki, S., Kanie, K., Watanabe, M., Abukawa, T., Yashiro, W., Takahashi, Y., Fukuyama, H., Muramatsu, A., Utsumi, W., Tanaka, H., Nishimori, N., Takahashi, M. & Kado, M. (2019). *AAPPS Bull.* **29**, 26–30.

Tamenori, Y. (2010). *J. Synchrotron Rad.* **17**, 243–249.

Tamenori, Y., Morita, M. & Nakamura, T. (2011). *J. Synchrotron Rad.* **18**, 747–752.

Thibault, P. & Menzel, A. (2013). *Nature*, **494**, 68–71.

Xiao, Q., Maclennan, A., Hu, Y., Hackett, M., Leinweber, P. & Sham, T.-K. (2017). *J. Synchrotron Rad.* **24**, 333–337.

Yu, E. Y., Pickering, I. J., George, G. N. & Prince, R. C. (2001). *Biochim. Biophys. Acta*, **1527**, 156–160.